Ionomer-Free Nickel-Iron bimetallic electrodes for efficient anion exchange membrane water electrolysis

E. López-Fernández [1,2], C. G. Sacedón[1], J. Gil-Rostra [2], J. P. Espinós [2], A. R. González-Elipe[2], F. Yubero[2**], A. de Lucas-Consuegra[1*]

[1] Department of Chemical Engineering, School of Chemical Sciences and Technologies, University of Castilla-La Mancha, Avda. Camilo José Cela 12, E-13071, Ciudad Real, Spain.

[2] Laboratory of Nanotechnology on Surfaces and Plasma, Institute of Materials Science of Seville (CSIC - Univ. Sevilla), Av. Américo Vespucio 49, E-41092 Sevilla, Spain

Corresponding authors:

*Antonio.LConsuegra@uclm.es

** Yubero@icmse.csic.es

Abstract

A bottleneck for the deployment of the Anion Exchange Membrane Water Electrolysis (AEMWE) is the manufacturing of efficient and long lasting anodes and cathodes for the cells. Highly performant bimetallic Ni/Fe catalyst films with various atomic ratios have been prepared by magnetron sputtering in an oblique angle configuration (MS-OAD) and used as anodes for AEMWE. Electrocatalytic experiments in a small three-electrode glass cell and a thorough analysis of the electrode properties with various physico-chemical characterization techniques have been used to select the nanostructured anode catalyst which, depicting an optimized Ni/Fe ratio, presents the maximum activity for the oxygen evolution reaction. These anode layers are then scale-up for their integration in an AEMWE cell where the influence of assembly conditions and the effect of adding an ionomer to the anodes have been studied. The obtained results have demonstrated the outstanding properties of the fabricated bimetallic films in terms of activity, stability, and operation under ionomer-free conditions. Current density values around 400 mA cm^{-2} at 2.0 V, much higher than those obtained with pure Ni, were obtained with an optimized membrane electrode assembly. The high yield obtained with these electrodes gains further relevance when considering that the current yield per unit mass of the anodic active phase catalyst (i.e., 1086 mA mg^{-1} at 2.0 V) is the highest among equivalent values reported in literature. The possibilities and prospects of the use of bimetallic catalyst films prepared by MS-OAD for AEMWE are discussed.

Keywords

1. Introduction

Electrochemical water splitting in basic conditions is a valuable procedure to generate hydrogen using sustainable energy sources [1,2]. In particular, Anion Exchange Membrane Water Electrolysis (AEMWE) has attracted much attention during the last years due to its advantages with respect to other electrolysis types, such as the reduction of membranes and catalysts cost as compared with Proton Exchange Membrane Water Electrolysis (PEMWE), or to lighten the problems associated to the formation of potassium carbonate in traditional alkaline electrolysis [3–5]. Nickel and nickel-transition metal based electrodes present a high catalytic activity in basic medium both for the oxygen and hydrogen evolution reactions (OER and HER) [6,7], although from the two the former is the most restrictive process due to its higher overpotential [8,9]. In this regard, it has been found that adding Fe to Ni catalysts decreases the OER overpotential [9], resulting in a highly active and low cost AEMWE electrocatalytic system compared with other non-platinum catalysts [1]. However, improving the electrode performance to make AEMWE a competitive technology entails further optimization of micro-structure, porosity, surface area, load and chemistry of active phase [6], while still reducing the overall cost of the electrolyser.

Besides other traditional fabrication techniques, we and other authors have demonstrated [10–16] that magnetron sputtering (MS) technology is a good choice for the fabrication of electrodes well suited to increase the performance of AEMWE cells. MS is a one-step method that simplify the electrode manufacture process [17]. It is a physical vapor deposition procedure that, if utilized in an oblique angle deposition configuration (MS-OAD), provides highly porous and nanostructured electrodes with low amounts of catalyst. MS is highly reproducible, scalable to large areas, does not produce residues (no liquid solvents are used as in other fabrication methods [18,19])

and work at room temperature [20,21]. In addition, a careful adjustment of the deposition geometry and the plasma gas pressure during the deposition process may render very porous electrodes with a strict control of composition, load and microstructure [20,22]. This technique is used to deposit thin films of pure metals from a single-target magnetron sputtering [23], metal alloys from more than one target or from a single-target with the desired composition [24,25] or oxides by means of an oxygen plasma discharge for the sputtering process [11]. Finally, MS provide other advantages as its high deposition rates that result in decreasing the time of electrode fabrication, or the high adhesion of films to the substrates [26]. In previous publications we have investigated the deposition by this method of mixed oxides and single metal electrodes. To advance in the integration of these electrodes in a real AEMWE, in this work we attempt the preparation of bimetallic thin film electrodes by MS-OAD. Although the electrodeposition fabrication method widely used for the preparation of metallic electrodes is a simple, low-cost and versatile technique [27], MS-OAD does not generate undesired waste residues. Among the new results of the present work, we also demonstrate the compatibility of this procedure with an efficient synthesis of nanostructure bimetallic electrodes providing outstandingly high current densities.

Traditional preparation methods of AEMWE electrodes using catalytic inks often involve the addition of polymeric organic ionomer binder molecules to increase the cell performance [3,28]. The ionomer function is to increase the amount of ion transport pathways at the reaction sites between the catalyst layer and the anion exchange membrane. It affects the gas permeability and, thanks to its charged functional groups, it facilities the exchange of water and OH^- anions at the catalyst surface [28,29]. However, ionomers can be also disadvantageous if, through electrostatic/covalent interactions, their charged groups occupy some catalyst active sites, leading to an increase in the

HER and OER potentials [28]. Over time, ionomers may also undergo chemical degradation, resulting in a deterioration of the effective catalyst-ionomer interface and, therefore, the electrochemically active electrode surface [30].

In the present work, we propose the development of ionomer-free Ni/Fe based anodes prepared by MS-OAD for their integration in highly efficient AEMWE cells. With this purpose, in a small three-electrode glass cell, we have firstly studied the OER performance of several Ni/Fe nanostructured anodes. A thorough structural, microstructural, chemical, and electrochemical characterization of electrodes with different atomic ratios was carried out by X-Ray Photoelectron Spectroscopy (XPS), Scanning Electron Microscopy (SEM), X-Ray Diffraction (XRD), Raman Spectroscopy, Energy Dispersive X-Ray (EDX) and Electrochemical Impedance Spectroscopy (EIS). As a result of this thorough characterization, it is realized that the metal character of the electrodes, their mixed oxide/hydroxide surface oxidation state and high surface area are key points accounting for their outstanding performance towards OER.

The best anode electrode composition and nanostructure has been selected and dimensions scale up for its integration in a membrane electrode assembly configuration (MEA) to study the influence of assembly conditions, electrolysis temperature, electrolyte concentration and ionomer addition. The obtained results have demonstrated the outstanding performance of the fabricated anodes in terms of activity and long-term stability, even in the absence of ionomer. The possibility to prepare by MS-OAD all kinds of nanostructured bi- or tri-metallic catalyst films at ambient temperature is highlighted in comparison with other traditional electrode preparation techniques such as ink spraying deposition [6], coprecipitation methods [31], electrodeposition [32], or

chemical growth of films [33], etc. that require various manufacturing steps, produce wastes, require ionomers or, simply, render a lower activity per unit mass.

2. Experimental

2.1. Fabrication of nanostructured electrodes

Anode bimetallic thin film electrodes made of Ni/Fe mixtures were prepared by MS at room temperature in an oblique angle deposition configuration (MS-OAD). According to **Figure S1 a)** in the Supporting Information (SI) a nickel target (GoodFellow Cambridge Ltd., 99.9 at. %, 50 mm diameter) with axially wrapped iron stripes (GoodFellow Cambridge Ltd., 99.5 at. %, 1.5 mm width, 0.25 mm thickness) was used for deposition (see **Figure S1 b)** of the SI file) [34]. The number of iron strips varied between one and five to obtain electrodes with different Ni/Fe atomic ratios. The sputtering target with wrapped iron stripes was operated in all cases using a pulsed DC power supply (AE Pinnacle+) at 150 W and a frequency of 120 kHz. Carbon paper substrates (TGP-H-90, Fuel cell Earth) were used as gas diffusion layer (GDL) to carry out the electrochemical experiments. Morphological characterization by Scanning Electron Microscopy (SEM) was carried out for films deposited on polished silicon wafer substrates. An *equivalent thickness* for the electrodes (540 nm for most films in this study) was obtained by cross-sectional SEM analysis of the films deposited onto the silicon substrates. The substrates, either carbon paper or silicon wafer, were placed on a circular sample holder of 10 cm diameter. This holder was positioned in an angle of ~78º with respect the centre of the magnetron target and was continuously rotating at 5 turns per minute to homogenise the microstructure of deposited films. Argon was used as plasma gas to obtain Ni/Fe metallic alloy electrodes. A flow of 30 sccm (standard cubic centimetres per minute) was dosed in the chamber yielding a process pressure of $5 \cdot 10^{-3}$ mbar. The base pressure in the system was $2 \cdot 10^{-6}$ mbar.

The cathodic catalyst layer consisted of nanostructured metallic Ni films prepared under the same conditions than the Ni/Fe anodic films, but with a bare nickel target (i.e., without iron stripes). For both anode and cathode, the deposition rate was 23.4 nm min^{-1} approximately.

Samples will be identified in the paper as follows: *XX-NiFe,* where *XX* refers the Ni/Fe at. ratio determined by Energy Dispersive X-Ray (EDX) Spectroscopy. Ni electrodes are designated by *Ni*. Thus, *10.1-NiFe* and *Ni* refer to electrodes with 10.1 Ni/Fe at. ratio and pure nickel, respectively. Note that XX-NiFe is just a way to label the manufactured samples according to their Ni/Fe stoichiometry determined by EDX. We denote as "as-prepared" electrodes those pristine samples that have not been used in any electrochemical test, and "used" samples those used in electrochemical experiments.

2.2. Physicochemical characterization of the electrodes

Scanning Electron Microscopy (SEM) was used to take normal and cross-section view images to characterize the microstructure and to determine the *equivalent thickness* of the films deposited on flat silicon substrates. A Hitachi S4800 field emission microscope operated at 2 keV was used for this purpose. In addition, Energy-Dispersive X-ray spectroscopy (EDX) mapping analysis was obtained using a Bruker X-Flash Detector 4010.

X-Ray Diffraction (XRD) analysis were performance in a Panalytical X'PERT PRO apparatus.

X-Ray photoelectron spectroscopy (XPS) characterization of surface chemical state was carried out for the electrodes before and after electrochemical cycling in the three-electrode glass cell. Measurements were taken with a SPECS PHOIBOS-100 spectrometer operated with unmonochromatic Mg Kα radiation as excitation source and

20 eV constant pass energy. The C 1s peak of the spurious contamination carbon adsorbed on the surface was taken at 284.5 eV and used as reference of the Binding Energy (BE) scale.

Raman spectra were obtained using a SENTERRA spectrometer with an excitation wavelength of 543 nm.

Inductively coupled plasma atomic emission spectroscopy (ICP-AES) analysis has been carried out using RL Liberty Sequential Varian ICP-AES to analyse the solution after experiments.

2.3. Electrocatalytic activity of the Ni/Fe anodes

To assess the influence of the Ni/Fe at. ratio on the OER performance of anodes, a series of electrochemical experiments were carried out in a three-electrode glass cell (i.e., half-cell configuration). This cell integrates a working anode (1.0 cm^2 geometric area), an Ag/AgCl reference electrode (KCl, 3M, Metrohm$^®$) and a platinum foil (Metrohm$^®$) counter electrode. A nitrogen gas flow was bubbled for at least 20 minutes prior to test the electrodes and then it was kept bubbling during the experiments.

The electrochemical characterizations, consisting of cyclic voltammetry (CV) and electrochemical impedance spectroscopy (EIS) analysis, were carried out with an Autolab PGSTAT30-ECOCHEMIE potentiostat/galvanostat. All measurements were performed at room temperature and 1.0 M KOH aqueous solution. CV scan rate was fixed at 20 mV s^{-1} and the voltage was ranged from 0 to +750 mV vs. Ag/AgCl. EIS measurements were carried out at +700 mV vs. Ag/AgCl with a potential perturbation amplitude of 10 mV, varying the AC frequency from 100 kHz to 10 mHz.

2.4. Electrocatalytic activity tests in a AEMWE cell

Electrodes prepared with the Ni/Fe stoichiometry depicting the highest OER yield with the three-electrode cell were scaled-up to a MEA configuration to study the influence of additional parameters (incorporation of ionomer, cell temperature, electrolyte concentration) to the performance of an AEMWE electrolyser cell (see the scheme of the experimental set up and details in **Figure S2** in the SI file). Thus, a *10.1-NiFe* electrode (catalyst load of 0.35 mg cm^{-2}, *equivalent thickness* 540 nm) was used as anode and a *Ni* electrode (load of 0.38 mg cm^{-2}, *equivalent thickness* 540 nm) as cathode. Catalyst films were deposited on carbon paper with a geometric area of 6.25 cm^2. The electrodes were separated by an anion exchange membrane (*Fumapem® FAA-3-50* supplied by Fuel Cell Store). The geometric area of the electrodes in the MEA was 5 cm^2 and the catalyst load was determined by weighing of the electrodes before and after the MS-OAD deposition.

Prior to use, the *Fumapem® FAA-3-50* anion exchange membrane was immersed in a 1.0 M KOH solution for, at least, 24 hours at room temperature (activation treatment). This membrane consisted of a very low resistance brownish-transparent foil (45-50 μm thick) of PET with Br$^-$ ions. An effect of this activation treatment is the replacement of Br$^-$ functional groups by OH$^-$ groups.

Typically, ionomers are mixed with the catalyst inks before their impregnation onto the corresponding gas diffusion layer [28,35,36], often with an optimised 20% ionomer/catalyst ratio [3,29,37]. Herein, to study the influence of ionomer addition, we have incorporated the ionomer on the anode surface after the catalyst deposition on the carbon paper GDL. A 10% *Fumion FAA-3* solution in N-Methyl-2-pyrrolidone (NMP) from Fuel Cell Store was selected as ionomer. Three situations have been explored: i) ionomer-free anodes; ii) anodes impregnated with previously mentioned optimised

ionomer/catalyst load (in our case dripping 4.4 mg of ionomer with a micropipette onto de catalyst deposit), labelled as *I/C=0.2* in the text); iii) anodes fully covered with ionomer solution (labelled *Ionom. Surf.* in the text). In all cases, the ionomer solvent was removed from the electrodes surface by drying in a muffle furnace at 210 °C for two hours.

The electrochemical measurements of the complete AEMWE cell were carried out with the Autolab potentiostat/galvanostat. In this case, experiments consisted of linear sweep voltammetries varying the potential from 1.0 to 2.2 V at various fixed temperatures between 30 and 60 ºC. Several electrolyte concentrations, 0.10, 0.15 and 1.0 M KOH, were used in both anode and cathode compartments. The scan rate was 5 mV s^{-1} and the torque applied to close the cell was varied between 1.0 and 3.0 Nm. In addition, the stability of the cell was investigated by constant-current chronopotentiometric experiments at 400 mA cm^{-2} for 2 days and cyclic voltammetry experiments (200 cycles, scan rate of 50 mV s^{-1}), both at 40 ºC.

EIS measurements were also performed for the MEA configuration (1.0 M KOH, 40 ºC). using the potentiostat/galvanostat. Data were collected at +2000 mV for a potential perturbation amplitude of 10 mV, varying the AC frequency from 100 kHz to 10 mHz.

3. Results and discussion

3.1. Composition and microstructure of Ni/Fe bimetallic electrodes

The surface microstructure of the Ni/Fe electrodes is exemplified with the SEM analysis of sample 10.1-NiFe before (**Figure 1 a)**) and after their use (**Figure 1 b)**) in a series of 25 cyclic voltammetries experiments. In both cases, a similar porous and rather homogeneous microstructure can be observed, without any appreciable degradation or delamination after use, clearly evidencing the great stability of the electrodes.

Furthermore, this stability can be confirmed because no traces of Fe and Ni have been observed after performing an ICP analysis of the solution after experiments. **Figure 1 c)** shows a cross-sectional image of the same catalyst film deposited onto a polished silicon substrate to measure its *equivalent thickness*. This image confirms that the film is composed of nanocolumns that, separated by large voids, provide a high porosity and straightforward liquid electrolyte accessibility to the whole electrode. This microstructure stems from the OAD conditions used for the fabrication and the resulting shadowing effects appearing in this variant of the magnetron sputtering technique [21]. **Figure S3** in SI file shows SEM images for others Ni/Fe at. ratio films deposited onto polished silicon substrates. It is apparent in these images that the addition of increasing amounts of Fe to the Ni based electrodes do not significantly modify the microstructure of the films.
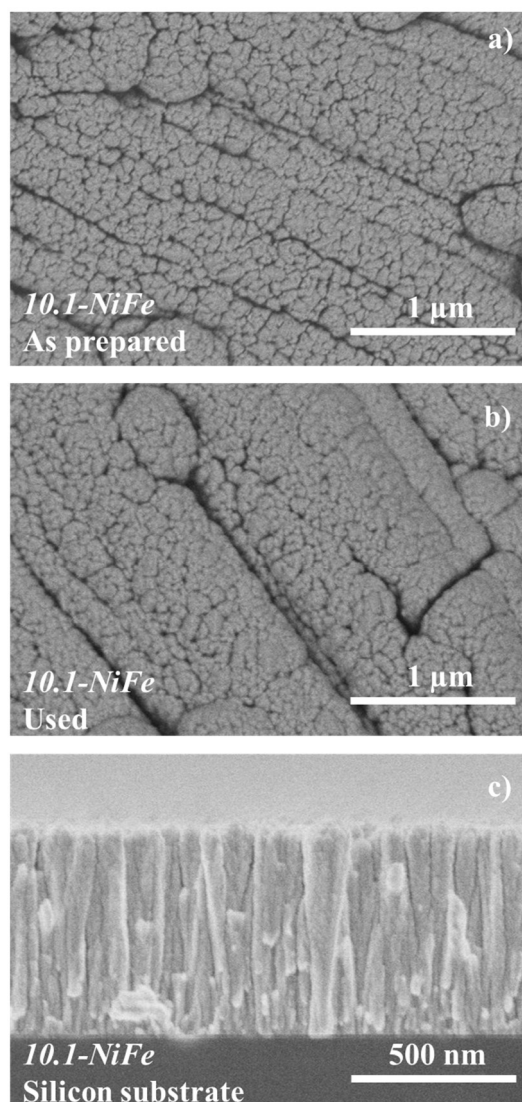
Figure 1. *SEM images in normal view of a) 10.1-NiFe sample as-prepared and b) after its usage in the three-electrode glass cell. c) Cross-sectional view SEM image of 10.1-NiFe sample supported on a polished silicon substrate.*

Table 1 gathers the values of *equivalent thickness* determined from the cross-sectional SEM images of the samples deposited on flat silicon substrates, as well as Ni/Fe at. ratio of *as-prepared* and used electrodes, determined by EDX and XPS analysis. The differences in at. ratios obtained for the same sample can be attributed to the different probing depth of these techniques (~3 nm depth for XPS and whole film thickness for

EDX). XPS data will be discussed later in *Section 3.3*. It is noteworthy that the *equivalent thickness* was similar for all electrodes (i.e., they had similar metal loadings), supporting that the electrochemical performances of electrodes with different Fe/Ni ratios can be properly compared.

It is also remarkable that the procedure utilized to control the Ni/Fe content in the electrodes (see experimental section) is quite versatile and permits a straightforward control of composition. Meanwhile, the elemental mappings in **Figure S4** of SI file obtained for sample *10.1-NiFe* confirms a homogeneous distribution of Ni and Fe across the whole deposited area of the electrode, supporting the existence of an atomic mixture of elements in the electrodes. The observation of oxygen in these maps, even if not homogeneously distributed, suggests that the surface of the bimetallic electrode nanostructures is oxidized because of its exposure to the air. This surface oxidation was confirmed by XPS as discussed below.

***Table 1**. Table of the physico-chemical characterization of the Ni/Fe anode electrodes.*

Sample	*Equivalent Thickness* / nm	Ni/Fe at. ratio		
		EDX	XPS	
			As-prepared	**Used**
20.6-NiFe	520	20.6	13.9	20.2
10.1-NiFe	540	10.1	8.3	11.5
7.1-NiFe	530	7.1	5.9	8.1
4.5-NiFe	550	4.5	4.6	6.4
2.9-NiFe	520	2.9	2.4	5.0

3.2. Ni/Fe atomic ratio and OER activity in a three electrode-cell configuration.

To study the influence of the Ni/Fe atomic ratio in the OER, electrochemical experiments were carried out in the three-electrode glass cell. **Figure 2 a)** shows a series of cyclic voltammetries recorded for electrodes with several Ni/Fe at. ratios. The curves are compared to that of a pure Ni anode with a similar thickness, taken as reference. Two well-defined peaks can be observed in the curves. An anodic peak (around 400 mV vs. Ag/AgCl), which is generally attributed to the electrochemical oxidation of $Ni(OH)_2$ to NiOOH and the corresponding cathodic peak attributed to the reversible reaction of NiOOH to $Ni(OH)_2$ [38,39]. Some modifications in these redox peaks are induced by the incorporation of iron to the electrodes. Changes consisting of a shift in the Ni^{+2}/Ni^{+3} oxidation potential to higher potentials values [40,41] are typically attributed to the formation of a Ni/Fe mixed oxyhydroxide [42,43]. In addition, the incorporation of iron has a positive effect in the OER activity, leading to a significant increase in current density values with respect to those obtained for a pure Ni anodic catalyst. This effect has been accounted for by the higher catalytic activity for OER of the Ni/Fe mixed oxyhydroxides than NiOOH [43]. This enhancement has been related to the substitution of Fe^{+3} for Ni^{+2} sites in $Ni(OH)_2$ [44,45] and NiOOH, leading to new Ni-O local environments with a superior activity for the OER [46]. Our results in **Figure 2 a)** show that the addition of increasing amounts of Fe to the Ni catalyst favours the OER activity until a plateau is reached for a Ni/Fe at. ratio around 10. It is likely that this value corresponds for the solubility limit of iron in the mixed oxide-hydroxide and that, when this limit is exceeded, a separated FeO_xH_y phase may segregate onto the surface [47]. In the course of these cyclic voltammetry experiments with the three-electrode cell, Tafel slopes were also calculated using the Butler-Volmer equation (see **Figure 2 b)**). According to this equation, smaller Tafel slope values can

be related with a higher electrocatalytic activity or a faster kinetics of the electron exchange process [48]. Figure 2 b) shows that a minimum value of 112 mV dec^{-1} is obtained for electrodes *10.1-Ni/Fe*. The slope value for this at. ratio is much smaller than that obtained for the Ni pure reference sample (161 mV dec^{-1}) and agrees with other published Tafel slope values reported in the literature for Ni/Fe anodes [49–51]. The improvement in the electrocatalytic activity due to the incorporation of iron also reflects in the onset potential values, which decrease from 530 mV vs. Ag/AgCl for pure Ni to 480 mV vs. Ag/AgCl for the *10.1-NiFe* anodic catalyst (see **Figure 2 c)** (note that these values are approximate since the onset partially overlaps with the anodic peak). In the same line, the overpotential value required to reach 10 mA cm^{-2} (see **Figure 2 d)**) was the lowest (i.e., 307 mV) for the *10.1-NiFe* anode, in good agreement with literature [1,52,53] (since overpotential values in our experiment are obtained in mV vs. Ag/AgCl, they had to be converted to mV vs. RHE, according to $E_{RHE} = E_{Ag/AgCl} + 0.059$ pH $+ E^0_{Ag/AgCl}$, where $E^0_{Ag/AgCl} = 0.1979$ V [54] taken a pH of 13.9 for the 1.0 M KOH solution). Furthermore, to facilitate comparison with other authors in the literature, **Figure S5** shows the cyclic voltammetry experiment carried out for the different electrodes expressed relative to the reversible hydrogen electrode (RHE) and current density values normalized per unit mass of anodic phase catalyst.
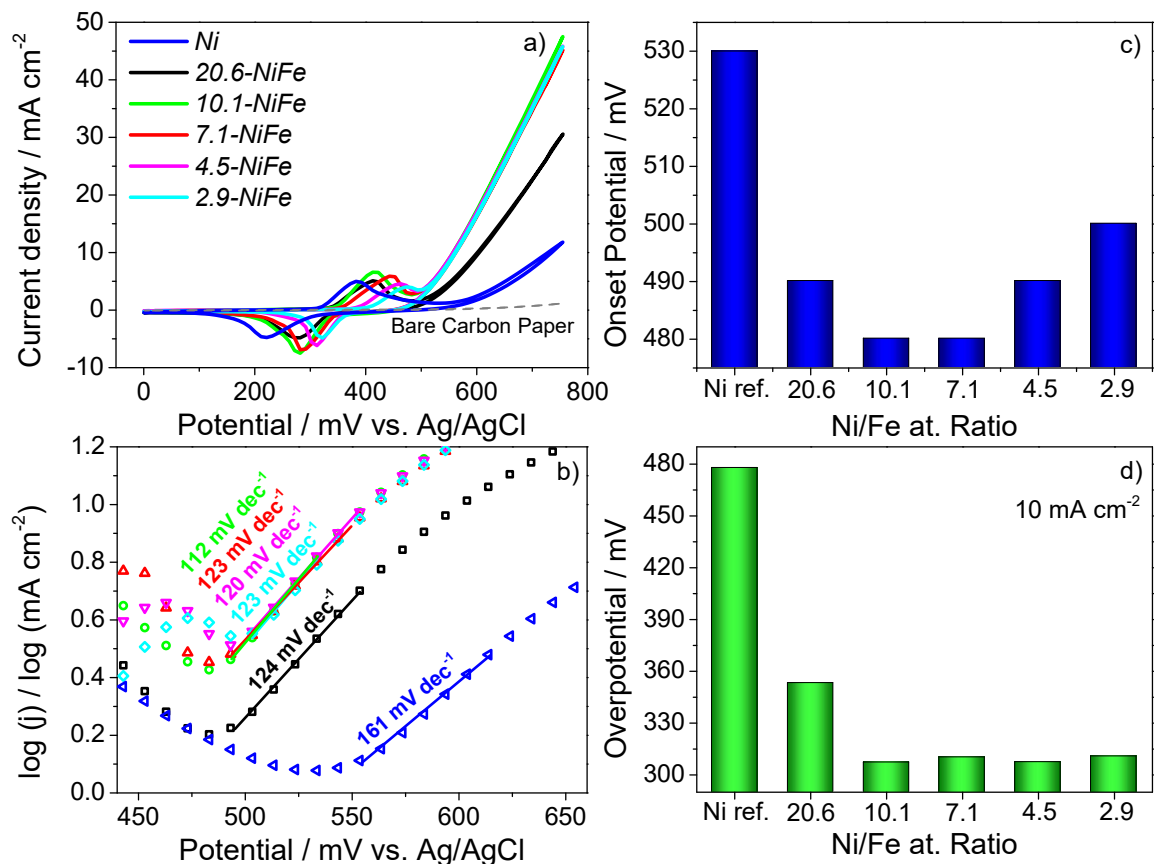
Figure 2. a) Cyclic voltammetry experiments carried out for electrodes with different Ni/Fe at. ratios in a three-electrode glass cell (room temperature, 1.0 M KOH electrolyte and 20 mV s^{-1} of scan rate). b) Corresponding Tafel plots (Tafel slopes obtained by linear regression of the initial rise of the OER are included). c) Onset potential values for OER and d) overpotential values evaluated at 10 mA cm^{-2} as a function of the Ni/Fe at. ratio in the samples.

The results above clearly demonstrate that, from the whole series of prepared electrodes, the *10.1-NiFe* anode presents the maximum OER activity. To further investigate the causes of the high electrocatalytic activity of this electrode, a comparative EIS analysis

was carried in the three-electrode glass cell at +700 mV. **Figure S6 a)** shows the Nyquist plots obtained for *Ni* and *10.1-NiFe* electrodes, as well as the equivalent $R_1(R_2C_1)$ electrical circuit that, according to literature, accounts well for the impedance behaviour of this type of anodes [10,55,56]. The table inserted in the figure shows the values of the electrical elements parameters obtained from the fitting of the experimental Z'' vs Z' curves. In this equivalent circuit, R_1 is usually related to an ohmic resistance between the surface of the working electrode and the reference electrode and is associated with the sum of contributions due to the resistance of the electrolyte, the electrode catalyst surface and the contacts [56]. Values of this resistance parameter are rather similar for the *Ni* and *10.1-NiFe* electrodes, though its slightly higher value for the former electrode points to a small increase of the resistance at the electrolyte-catalyst interface in this case. On the other hand, R_2 is commonly associated with the charge transfer resistance through the electrode during the OER [56]. The observed decrease of R_2 by a factor of more than two for the *10.1-NiFe* electrode with respect to pure nickel can be related with the highest electrocatalytic activity of the bimetallic electrodes [57], agreeing with similar tendencies found in other studies [55].

The EIS analysis can be also utilized to deduce other activity-related parameters for the electrode catalysts. Watzele et al. [58] have recently proposed a procedure to determine the Electrochemical Surface Area (ECSA) using an alternative interpretation of *Nyquist* plots. Using the same model (see details in the SI, **Figure S6 b)** for a detailed calculation of this parameter), we have calculated the ECSA values for the *Ni* and for *10.1-NiFe* electrodes and got values of 6.13 and 10.13 cm^2, respectively. These values suggest that the surface available for the OER reaction will be higher for the *10.1-NiFe* electrode. Remarkably, it is also higher than others values reported in the literature for Ni-Fe electrode catalysts prepared by other methods [59].

3.3. Chemical and structural characterization of Ni/Fe electrodes before and after cyclic voltammetry analysis.

Chemical compositions and oxidation states at the surface of electrode samples were investigated by XPS analysis. **Figures 3 a-c)** show the Ni 2p, Fe 2p and O 1s spectra obtained for pristine samples with different Ni/Fe at. ratios. **Figures 3 d-f)** show a comparison of Ni 2p, Fe 2p and O 1s spectra for the *10.1-NiFe* electrode in its as prepared state and after electrochemical cycling in the three electrode cell. Since electrodes were deposited by MS from metallic targets using pure Ar as plasma gas, the observation of oxygen by XPS must be attributed to the surface oxidation upon exposure to ambient air [60]. In this regard, the observation in all samples of Ni 2p shoulders at 869.8 and 853.0 eV in Figure 3 a) due to Ni^0 [61] confirms that surface oxidation has not progressed to the interior of the films, which must have preserved a metallic character. Ni 2p spectra are dominated by two satellite peaks at 880.5 and 861.7 eV and two main peaks at 873.5 and 855.9 eV corresponding to Ni $2p_{1/2}$ and Ni $2p_{3/2}$ levels, respectively, that must be attributed to Ni^{+2} species [62]. In the Ni/Fe bimetallic electrodes, the Fe 2p spectra depict two peaks at 725.0 and 711.4 eV corresponding to Fe $2p_{1/2}$ and Fe $2p_{3/2}$ core levels of Fe^{+3} [63]. Meanwhile the O 1s spectra depict a contribution at 531.5 eV binding energy, attributed to the OH^- groups, and another at 530.2 eV attributed to O^{2-} groups [10]. Although differences depending on sample are observed in the relative intensity of these two contributions (c.f., Figure 3 c)), no clear conclusions can be derived from this observation for samples exposed to air.

However, the comparison in Figures 3 d)-f) of the spectra of the as-prepared and used *10.1-NiFe* sample does provide a valuable information regarding the effect electrochemically cycling on the surface state of samples. For example, the spectra of

the used sample lack any Ni^0 contributions, indicating that surface oxidation has progressed beyond the probing depth of XPS (3-4 nm). A similar effect was observed in a previous study with pure Ni [10]. Thus, by XPS analysis, Ni^{+2} and Fe^{3+} seem to be the sole cationic species present at the surface of the used samples, being likely that these cationic species were involved in the OER. Meanwhile, the O 1s spectrum in the used sample appears dominated by a single band due to OH^- groups (i.e. BE 531.5 eV). This agrees with the use of potassium hydroxide solution as electrolyte and strongly supports the involvement of a hydroxide and/or oxyhydroxide of Ni and Fe in the OER [10,11]. Spectra for the other samples after their use in the three-electrode glass cell depict a similar evolution of chemical states (see **Figure S7** in the SI file) as those reported in Figure 3 for sample *10.1-NiFe*. However, it is interesting that the Ni/Fe ratio at the surface of all samples increases after electrochemically cycling in the basic electrolyte (c.f., Table 1). This feature suggests that the surface of electrode experiences a partial enrichment of Ni at the outmost layers during cycling. Similar surface enrichment phenomena have been already observed in previous studies on the OER with Co/Cu oxide electrodes prepared by MS-OAD [11]. For sample *10.1-NiFe*, the Ni/Fe determined after cycling is 11.5, relatively close to the nominal composition determined by EDX for the whole electrode. The possibility that during cycling there can be segregations and mobilization of elements at the surface will be further discussed below when presenting the XRD characterization of the investigated samples.
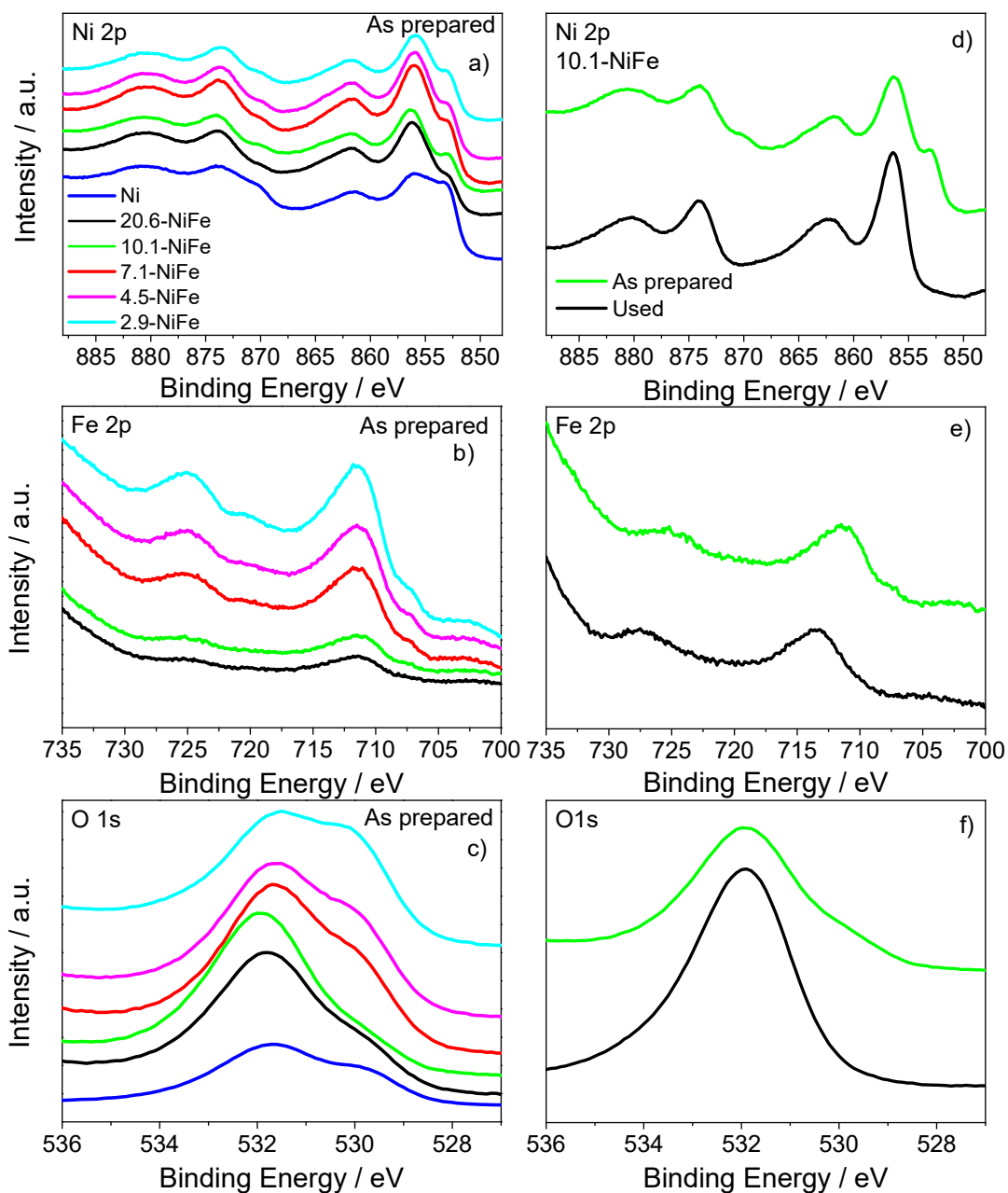
Figure 3. *a) Ni 2p, b) Fe 2p and c) O 1s XPS spectra of several Ni/Fe at. ratio electrodes in their pristine state; d) Comparison of the Ni 2p, e) Fe 2p and f) O 1s spectra of 10.1-NiFe sample before and after electrochemical cycling in the three-electrode glass cell.*

A XRD analysis (see **Figure 4**) of the as prepared Ni/Fe bimetallic anodes has been carried out to determine their crystallographic structure. In addition, a comparative analysis has been carried out for sample *10.1-NiFe* before and after its use as OER electrode. The series of diffractograms in **Figure 4 a)** depict a characteristic very intense diffraction peak at ~54.6 º attributed to the carbon paper used as substrate [64] that is labelled as [a] in the figure. In addition, two smaller diffraction peaks at approximately ~44.5 and ~51.9 º, labelled as [b] in the figure, can be attributed to metallic nickel or a Ni containing alloy [65]. An enlarged view of these peaks is included in **Figure S8** in the SI file to clearly show the evolution of the intensity and width of this peak depending on sample. Thus, it is apparent that the intensity of these peaks decreases and their width increases for lower Ni/Fe ratios, as expected if Fe has become incorporated within the fcc structure of Ni, forming a kind of alloy (a certain displacement of the peak at 44.5 º further supports this assumption) [66–68]. Meanwhile, quite small, but still observable peaks appear at ~42.6 and ~43.1 º (labelled as [c] and [d]) that can be attributed to NiO and NiOOH [69]. It is noteworthy in this regard the observation of a small diffraction peak at ~37.2 º (labelled as [h]) both in the as prepared and used samples, that can be attributed to $NiFe_2O_4$ [70]. Peaks corresponding to the oxyhydroxides of Fe, ~36.0, ~36.5, ~31.7 and ~41.4 º [71,72], labelled as [f] and [g]), appear rather intense in the *10.1-Ni/Fe* used sample and must be linked to the effect of the KOH electrolyte in the chemical state of elements at the surface of samples. Interestingly, the diffraction peaks at ~34.9 and ~40.5 º, likely due to Fe_2O_3 [73] (labelled as [e]), only appear in the *10.1-Ni/Fe* used electrode. In this case, two new peaks attributed to residual KOH were observed at ~32.4 and ~39.4 º [74] (labelled as [i]). The lack of XRD peaks attributable to metallic Fe confirms the incorporation of Fe into the Ni structure in the form of a kind of metal alloy. Overall,

this XRD analysis shows that bimetallic electrodes consist of a metallic alloy, which can be partially oxidized in agreement with the surface oxidation observed by XPS, particularly in the used samples. The observation of XRD peaks due to segregated iron oxides and hydroxides confirms the evolution of the surface of samples with the formation under certain conditions of a mixture of separated Ni and Fe oxidized phases. In agreement with the electrochemical analysis in Figure 2 this effect, though, should be lower in sample *10.1-NiFe*.
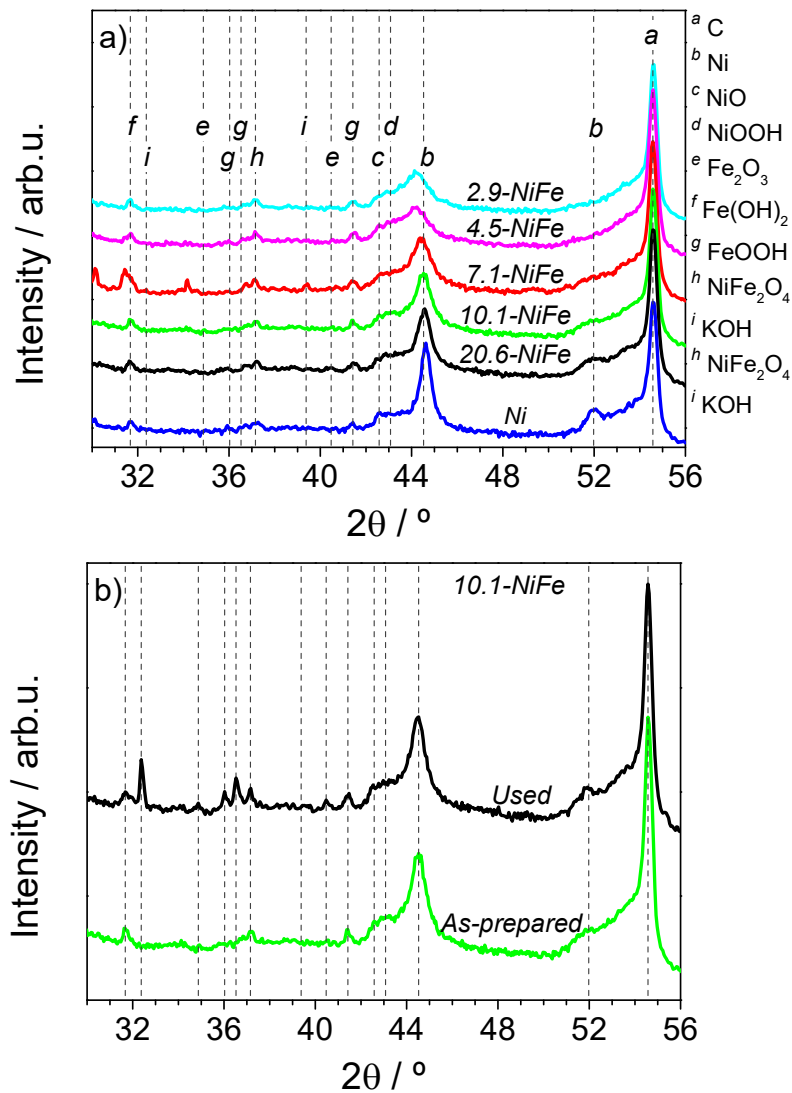
Figure 4. *X-Ray diffractograms of a) several as prepared Ni/Fe electrodes and b) as-prepared and used 10.1-NiFe sample.*

The Raman analysis of samples confirms the previous view and support the existence of a mixed oxide/hydroxide phase in the Ni/Fe electrodes. The spectrum of the Ni sample in **Figure S9** of the SI file shows a characteristic peak at 521 cm^{-1} attributed to Ni^{III}-O lattice vibrations in NiOOH [75]. In comparison, the spectra of *4.5-NiFe* and *10.1-NiFe* electrodes show a new characteristic peak shifted positively with respect to the peak due to Ni^{III}-O vibrations. This additional band confirms the incorporation of Fe atoms in the structure through the formation of Ni(Fe)O$_x$H$_y$ [75,76]. We assume that this phase formed at the surface is responsible for the higher performance of Ni/Fe in comparison with that of Ni electrodes. For the metallic Ni/Fe electrodes prepared by MS-OAD in this work, this enhancement of surface reactivity combines with the metallic character of the bulk of the catalyst film, a feature that diminishes the electrical resistance of the electrode, further contributing to the observed enhancement in reactivity.

It is also relevant in this study that the SEM analysis of the used electrodes revealed a similar morphology and microstructure than that of the as prepared electrodes (c.f., Figure 1a) and b)). This observation discarded any possible delamination of the catalyst in the used electrodes and confirmed the stability of bimetallic electrodes even if a partial oxidation occurs at their surface during the OER process.

3.4. Electrode performance in the AEMWE cell configuration.

The enhanced electrochemical activity of the bimetallic catalyst films, particularly that of sample *10.1-Ni/Fe,* determined in the three electrode cell justifies their integration in a full AEMWE cell to determine whether this high activity remains under close to real

conditions of operation. From the point of view of electrode manufacturing, this integration possesses some challenges related with the increase in the electrode area, the need to keep the microstructure and chemical behaviour described in the previous sections and the preservation of their high performance at temperatures and working conditions different than in the three-electrode cell.

3.4.1. Influence of working parameters in the performance of the AEMWE cell

The *10.1-Ni/Fe* electrode type was incorporated in a full AEMWE cell to prove its reliability under close to real operation conditions. For this purpose, a MEA composed by sample *10.1-NiFe* as anode, *Ni* as cathode (in previous study, we showed that MS-OAD nickel electrodes act as optimum cathodes for the production of hydrogen [10]) and a *Fumapem®* separation membrane were assembled as explained in the experimental section. In the resulting AEMWE cell we studied the influence of several operation parameters, namely the torque applied for cell assembly, the working temperature, and the KOH concentration. **Figure S10** in the SI file shows that for low assembly torque values (<2 Nm), current density increases with assembly pressure likely due to contact improvement between membrane and catalysts. For assembly pressures resulting from torques higher than 2.5 Nm, the observed decrease in current density was attributed to a decrease in gas transport through the carbon paper and the partial coverage of electrode surface by gas bubbles [77]. A torque of 2.5 Nm was therefore taken as the optimum value for cell assembly and this value was applied for the characterization studies as a function of temperature and KOH concentration.

Figure 5 a) shows that global performance improves with temperature. This is a well-known effect in AEMWE usually attributed to an increase in the kinetics of the electrochemical reactions and in the mobility of hydroxyl ions [78]. Assuming an Arrhenius behaviour for the electrochemical reaction [79], the activation energy (E_a) of

the process can be calculated from the slope of the plot of the logarithm of current density vs. the inverse of the temperature. This slope corresponds to E_a/R, with R the gas constant value of 8.314 J (mol K)$^{-1}$, and renders E_a values of 19.1, 20.3 and 20.9 kJ mol^{-1} for operating potentials of 1.9, 2.0 and 2.1 V, respectively. These activation energies are similar to other values reported in the literature for the same process [79,80].

Figure 5 b) accounts for the influence of the KOH electrolyte concentration in the polarization curves. At low KOH concentration (i.e., 0.1 M), when the process is kinetically controlled [81], the electrolyte concentration does not significantly affect the polarization curves. However, at high KOH concentrations the current density increases for V>1.9 volt, pointing to that an increase in the ion conductivity through the membrane contributes to diminish the ohmic overpotential required for the OER [82].

Long-term stability of the AEMWE cell was also analysed monitoring its response along a chronopotentiometry experiment. For a constant current of 400 mA cm^{-2}, the curve reported in **Figure 5 c)** evidences a slight decrease in the cell potential over time (0.3 % V h^{-1}). This slight decrease in performance is similar to that reported in other studies with anodes prepared by MS [10,12], but lower than results corresponding to cells incorporating anodes prepared using other methods [83–85].
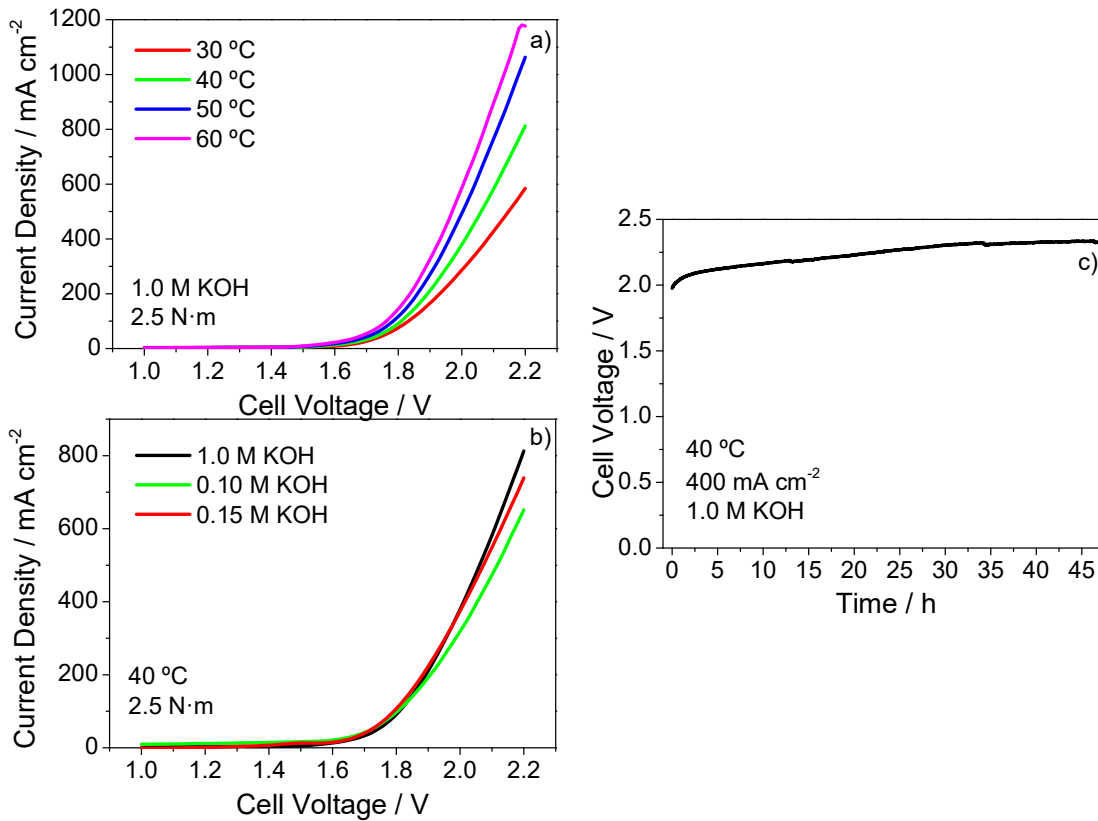
Figure 5. *Polarization curves obtained for a MEA integrated by 10.1-NiFe and Ni as anodic and cathodic electrodes, respectively. a) For various operation temperatures at an assembly torque of 2.5 Nm, 1.0 KOH. b) For different electrolyte concentrations at 40 °C and 2.5 Nm. c) Constant-current chronopotentiometry curve at a fixed current of 400 mA cm^{-2}, 40°C, 1.0 M KOH, and an assembly torque of 2.5 Nm.*

3.4.2. Influence of ionomer addition to the electrodes in the performance of AEMWE cell

As previously mentioned, the addition of an ionomer is commonly used to increase the performance of AEMWE electrolyzers [28]. When applying traditional electrode preparation methods, the ionomer is added to the catalyst ink and as binder and to

favour the ion transfer transport up to the reaction sites. Conversely, the ionomer can be added after the electrode manufacturing, in most cases also resulting in an increase in performance [86,87]. Considering that no delamination of the active catalyst layer has been detected after long-term operation, it appears that MS electrodes do not require any binding agent to fix the catalyst layer to the GDL support. Therefore, we hypothesize that the addition of ionomer to the electrodes might principally contribute to favour the ion diffusion. To check possible improvements in performance due to ionomer addition, three different cell configurations have been tested as explained in **Section 2.4** in the Experimental Part. In general, the amount of added ionomer is optimized to maximize the electrochemical yield of the cells, with an Ionomer/Catalyst (I/C) ratio of 0.2 being a common value in various studies on the subject [3,29,37]. However, the AEMWE cells incorporating MS-OAD electrodes seem to behave differently. Linear sweep voltammetries in **Figure 6 a)** show a maximum performance for sample *10.1-NiFe* without ionomer, and that the electrochemical response is not affected by the addition of ionomer for a I/C ratio of 0.2 (i.e., 4.4 mg of ionomer). Moreover, the performance drastically decreased adding more ionomer to cover the entire surface of the catalyst. A similar effect can be deduced from **Figure 6 b)**, where long-term chronopotentiometry stability tests show that, for a constant current density of 400 mA cm^{-2}, a lower potential is required for the electrodes without ionomer. Moreover, for long operation times, the cell voltage increase was 0.3 % V h^{-1} for the electrode without ionomer and 0.6 % V h^{-1} and 0.9 % V h^{-1} for the electrode with I/C=0.2 and its full surface covered with ionomer, respectively. We believe that the inefficiency of ionomers with the MS-OAD electrodes is related with a morphology where diffusion constrains towards OH$^-$ seem to be unimportant and the fact that the ionomer is added once the electrode has been prepared and will likely cover part of the catalyst active sites [29]. This hypothesis was

confirmed through various electrochemical tests as, for example, the fact that while the cyclic voltammetry curves did not change after 200 cycles with the *10.1-NiFe* cell electrode, slight and high increases in density current were found, respectively, for the electrodes covered with ionomer at I/C=0.2 or total coverage, respectively (see **Figure S11** in the SI file). This behaviour is consistent with a progressive dragging out of ionomer molecules from the electrode surface after the successive cycles. The detrimental role of the ionomer also agrees with the SEM observations (see **Figure S12** in the SI file) showing that ionomer agglomerates form onto the Ni/Fe nanocolumnar structure and likely block some of the catalyst active sites. Electrochemical evidence of this blocking effect was provided by the EIS analysis of the complete MEAs. **Figure 6 c)** shows the measured Nyquist plots for the three MEAs and the equivalent circuit (inset in the figure, similar to ref [42]) utilized to retrieve resistance parameters. In this representation, the intersection to the X axis at high frequencies is related to the ohmic resistance of the membrane (R_{EL}) or with the electrolyte resistance associated to the availability of OH^- ions [42]. The charge transfer resistance (R_{ct}) is obtained by the difference between the two intersection at a high and low frequencies (diameter of the semicircle) and is related to the polarization resistance or to the kinetics of the electrochemical reactions [10,42]. Fitting values are included in the table inserted in the figure. The obtained values are similar to values reported for other systems including ionomers [42] and can be easily interpreted assuming that the relatively higher R_{EL} values found for the ionomer containing electrodes respond to an increase of thickness of the catalyst-ionomer layer. Similarly, the lowest R_{ct} value found for the *10.1-NiFe* ionomer-free electrode, agrees with the little restrictions to the transfer of charge through the catalyst film in this case.
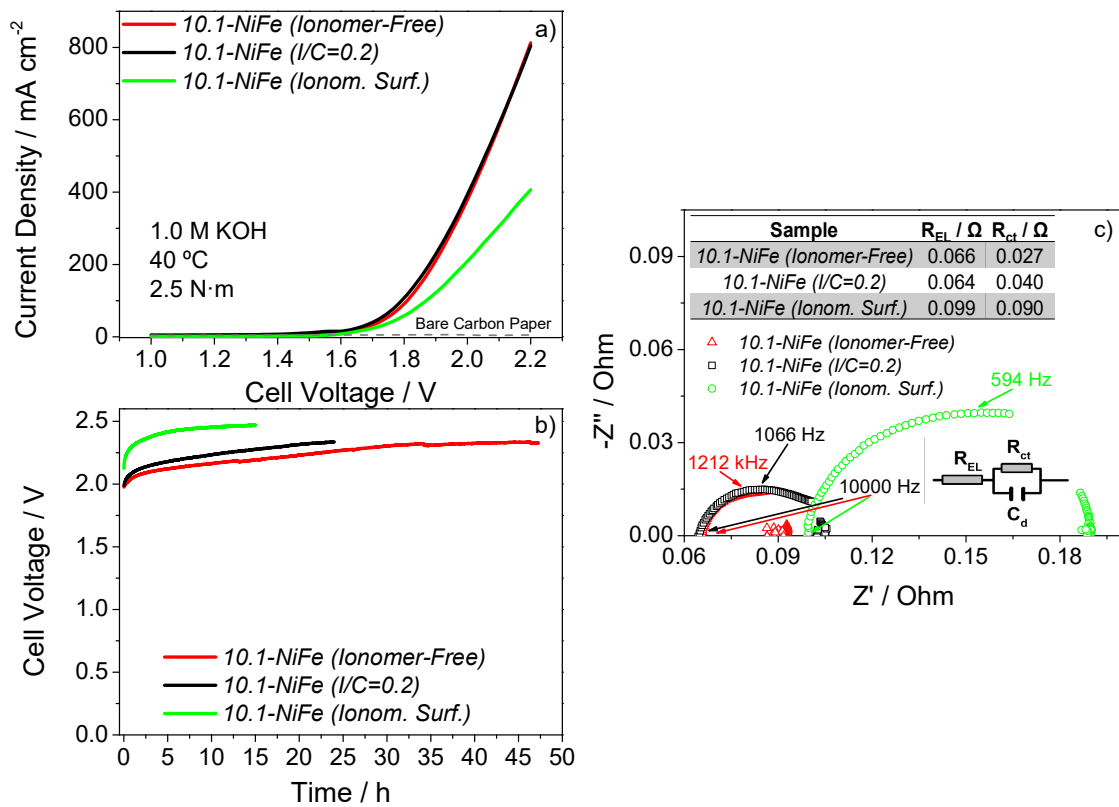
Figure 6. *Effect of the addition of ionomer to a 10.1-NiFe electrode in a MEA assembly (1.0 M KOH solution, temperature of 40 ℃ a) polarization curves for 10.1-NiFe electrodes with or without ionomer impregnation, b) Idem, constant-current chronopotentiometry experiments (@400 mA cm⁻², c) idem, impedance spectra of the cell evaluated at 2.0 V.*

3.4.3. Comparison with other AEMWE cells

To put in context the AEMWE electrolyzer performance with MS-OAD electrodes, we compare the obtained results with others recently reported in the literature. A first remark is that, although the current density value obtained here (i.e., 400 mA cm⁻² at 2.0 V) is smaller than reported values for electrodes prepared with an ink spraying coating process, e.g. 1900 [42], 720 [88] or 1400 mA cm⁻² [3], it is higher than most published

data in the literature, where values ranging between 140 and 250 mA cm^{-2} [86,89,90] are rather common.

However, the performance of the NiFe anodes developed here gains a particular relevance when expressing their activity in terms of current density per amount of catalyst (specific activity). **Figure 7** summarizes some of the results mentioned above formulated in these units. It is noteworthy that the current yield per amount of *10.1-NiFe* catalyst (1086 mA mg^{-1}) is superior to any other of the values reported in the literature for Ni/Fe [42,86], Ni [10,88–90], cobalt-based oxides [11,29,91,92] or those obtained with a novel IrO$_2$ anodes [3,86,93]. Moreover, this result is especially outstanding considering that the AEMWE electrodes in this work are ionomer-free and therefore simpler from the point of view of their manufacturing and processing.
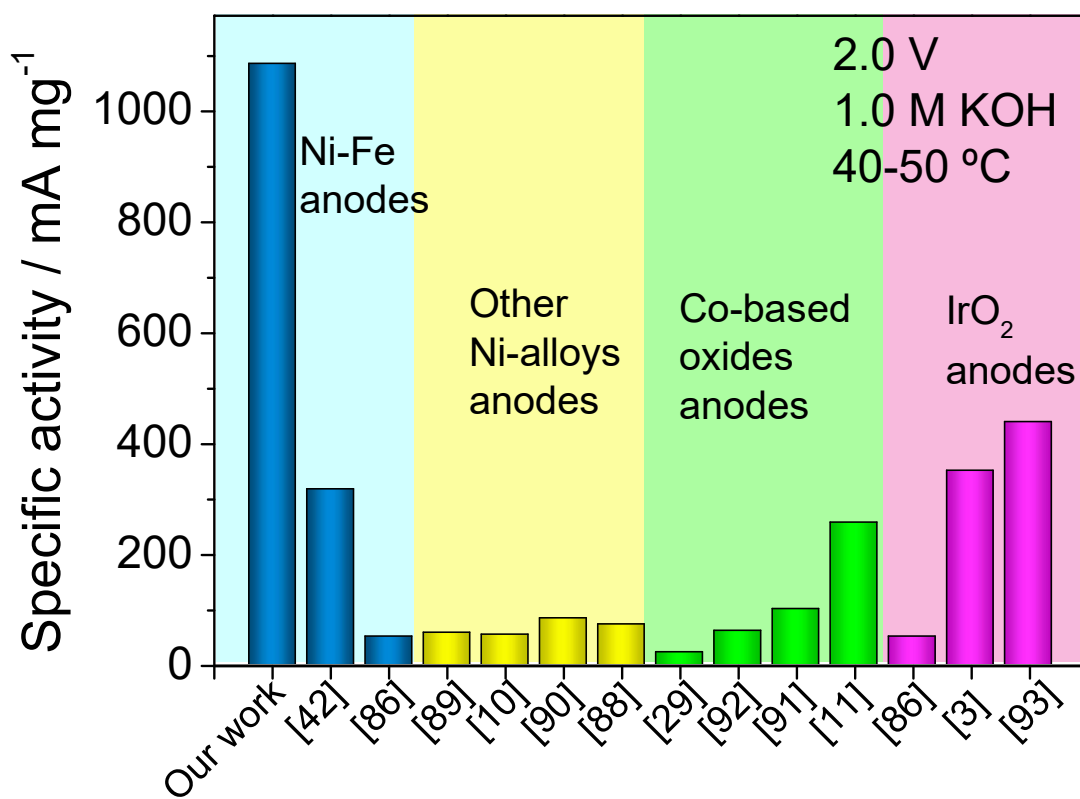
Figure 7. *Electrochemical performance of our 10.1-NiFe anode based AEMWE, characterised by its specific activity, compared to other reported results from literature.*

4. Conclusions

The previous results and discussion have pointed out that the MS-OAD technique is a suitable method of fabrication of Ni and Ni/Fe anodes for water electrolysis cells. Incorporation of Fe within Ni based anodes improves the OER performance and we have demonstrated that a maximum performance is reached for a Ni/Fe at. ratio of around ten (400 mA cm^{-2} at 2.0 V). The modifications introduced in this physical vapour deposition procedure, in terms of deposition geometry and other operating conditions render nanocolumnar thin films with a high porosity and good conformality

onto the carbon paper used as GDL support. This has been demonstrated through an outstanding electrochemical response, particularly for the electrodes with the optimum composition. These electrodes presented a high reaction yield, good repetitively upon cycling and long-term stability, features that have been accounted for by the particular microstructure and high surface area of these electrodes and the mixing at atomic scale of their constituent elements both before and after their activation to generate a catalytically active oxide/hydroxide surface layer.

The good properties of the electrodes when tested in a three-electrode laboratory cell, have been confirmed upon their integration in a MEA for their testing in a complete AEMWE cell. In particular, it has been demonstrated that the addition of ionomers, a critical issue for most conventional AEMWE cells, does not improve the performance of MS-OAD Ni/Fe electrodes, thus simplifying the manufacture and integration of cells and reducing the costs and other problems (stability, reproducibility) associated with the incorporation of this kind of additives.

The high stability and specific activity (1086 mA mg^{-1} at 2.0 V) depicted by the MEA integrated *10-NiFe* anode in comparison with other results recently reported in the literature, confirm the MS-OAD technique as an appropriate method to fabricate ionomer-free nanostructured electrodes for AEMWE.

REFERENCES

[1]   D. Lim, E. Oh, C. Lim, S.E. Shim, S.-H. Baeck, Bimetallic NiFe alloys as highly efficient electrocatalysts for the oxygen evolution reaction, Catal. Today. 352 (2020) 27–33. https://doi.org/10.1016/j.cattod.2019.09.046.

[2]   L. Xu, L. Cao, W. Xu, Z. Pei, One-step electrosynthesis of NiFe-NF electrodes for highly efficient overall water splitting, Appl. Surf. Sci. 503 (2020). https://doi.org/10.1016/j.apsusc.2019.144122.

[3]   J.E. Park, S.Y. Kang, S.-H. Oh, J.K. Kim, M.S. Lim, C.-Y. Ahn, Y.-H. Cho, Y.-E. Sung, High-performance anion-exchange membrane water electrolysis, Electrochim. Acta. 295 (2019) 99–106. https://doi.org/https://doi.org/10.1016/j.electacta.2018.10.143.

[4]   A.K. Niaz, A. Akhtar, J.-Y. Park, H.-T. Lim, Effects of the operation mode on the degradation behavior of anion exchange membrane water electrolyzers, J. Power Sources. 481 (2021) 229093. https://doi.org/https://doi.org/10.1016/j.jpowsour.2020.229093.

[5]   C.-Y. Kwon, J.-Y. Jeong, J. Yang, Y.S. Park, J. Jeong, H. Park, Y. Kim, K.-S. Moon, S.M. Choi, Effect of Copper Cobalt Oxide Composition on Oxygen Evolution Electrocatalysts for Anion Exchange Membrane Water Electrolysis, Front. Chem. 8 (2020). https://doi.org/10.3389/fchem.2020.600908.

[6]   A. Lim, H. Kim, D. Henkensmeier, S. [Jong Yoo], J. [Young Kim], S. [Young Lee], Y.-E. Sung, J.H. Jang, H.S. Park, A study on electrode fabrication and operation variables affecting the performance of anion exchange membrane water electrolysis, J. Ind. Eng. Chem. 76 (2019) 410–418. https://doi.org/https://doi.org/10.1016/j.jiec.2019.04.007.

[7]   T. Rauscher, C.I. Bernäcker, U. Mühle, B. Kieback, L. Röntzsch, The effect of Fe as constituent in Ni-base alloys on the oxygen evolution reaction in alkaline solutions at high current densities, Int. J. Hydrogen Energy. 44 (2019) 6392–6402. https://doi.org/https://doi.org/10.1016/j.ijhydene.2019.01.182.

[8]   N.-T. Suen, S.-F. Hung, Q. Quan, N. Zhang, Y.-J. Xu, H.M. Chen, Electrocatalysis for the oxygen evolution reaction: recent development and future perspectives, Chem. Soc. Rev. 46 (2017) 337–365. https://doi.org/10.1039/C6CS00328A.

[9]   Y. Cheng, S.P. Jiang, Advances in electrocatalysts for oxygen evolution reaction of water electrolysis-from metal oxides to carbon nanotubes, Prog. Nat. Sci. Mater. Int. 25 (2015) 545–553. https://doi.org/https://doi.org/10.1016/j.pnsc.2015.11.008.

[10]   E. López-Fernández, J. Gil-Rostra, J.P. Espinós, A.R. González-Elipe, A. de Lucas Consuegra, F. Yubero, Chemistry and Electrocatalytic Activity of Nanostructured Nickel Electrodes for Water Electrolysis, ACS Catal. 10 (2020) 6159–6170. https://doi.org/10.1021/acscatal.0c00856.

[11]   E. López-Fernández, J. Gil-Rostra, J.P. Espinós, A.R. González-Elipe, F. Yubero, A. de Lucas-Consuegra, $Cu_xCo_{3-x}O_4$ ultra-thin film as efficient anodic catalysts for anion exchange membrane water electrolysers, J. Power Sources. 415 (2019) 136–144. https://doi.org/10.1016/j.jpowsour.2019.01.056.

[12]   E. López-Fernández, J. Gil-Rostra, C. Escudero, I.J. Villar-García, F. Yubero, A. de Lucas Consuegra, A.R. González-Elipe, Active sites and optimization of mixed copper-cobalt oxide anodes for anion exchange membrane water electrolysis, J. Power Sources. (2020).

https://doi.org/10.1016/j.jpowsour.2020.229217.

[13] Q. Zhang, Z.D. Wei, C. Liu, X. Liu, X.Q. Qi, S.G. Chen, W. Ding, Y. Ma, F. Shi, Y.M. Zhou, Copper-doped cobalt oxide electrodes for oxygen evolution reaction prepared by magnetron sputtering, Int. J. Hydrogen Energy. 37 (2012) 822–830. https://doi.org/https://doi.org/10.1016/j.ijhydene.2011.04.051.

[14] A.I. Inamdar, H.S. Chavan, S.M. Pawar, H. Kim, H. Im, NiFeCo oxide as an efficient and sustainable catalyst for the oxygen evolution reaction, Int. J. Energy Res. 44 (2020) 1789–1797. https://doi.org/https://doi.org/10.1002/er.5026.

[15] M. Cano, F.J. Garcia-Garcia, D. Rodríguez-Padrón, A.R. González-Elipe, J.J. Giner-Casares, R. Luque, Ultrastable $Co_xSi_yO_z$ Nanowires by Glancing Angle Deposition with Magnetron Sputtering as Novel Electrocatalyst for Water Oxidation, ChemCatChem. 11 (2019) 6111–6115. https://doi.org/10.1002/cctc.201901730.

[16] J. Lian, F. Zhang, S. Lu, W. Jiang, Q. Hu, D. Li, B. Zhang, Amorphous Fe−Co−P−C Film on a Carbon Fiber Paper Support as an Efficient Electrocatalyst for the Oxygen Evolution Reaction, ChemElectroChem. 6 (2019) 3976–3981. https://doi.org/10.1002/celc.201900978.

[17] Q. Wang, Z. Zhao, H. Li, J. Zhuang, Z. Ma, Y. Yang, L. Zhang, Y. Zhang, One-step RF magnetron sputtering method for preparing $Cu(In, Ga)Se_2$ solar cells, J. Mater. Sci. Mater. Electron. 29 (2018) 11755–11762. https://doi.org/10.1007/s10854-018-9274-y.

[18] D. Li, E.J. Park, W. Zhu, Q. Shi, Y. Zhou, H. Tian, Y. Lin, A. Serov, B. Zulevi, E.D. Baca, C. Fujimoto, H.T. Chung, Y.S. Kim, Highly quaternized polystyrene ionomers for high performance anion exchange membrane water electrolysers,

Nat. Energy. 5 (2020) 378–385. https://doi.org/10.1038/s41560-020-0577-x.

[19] Y.S. Park, J. Yang, J. Lee, M.J. Jang, J. Jeong, W.-S. Choi, Y. Kim, Y. Yin, M.H. Seo, Z. Chen, S.M. Choi, Superior performance of anion exchange membrane water electrolyzer: Ensemble of producing oxygen vacancies and controlling mass transfer resistance, Appl. Catal. B Environ. 278 (2020) 119276. https://doi.org/https://doi.org/10.1016/j.apcatb.2020.119276.

[20] A. Barranco, A. Borras, A.R. Gonzalez-Elipe, A. Palmero, Perspectives on oblique angle deposition of thin films: From fundamentals to devices, Prog. Mater. Sci. 76 (2016) 59–153. https://doi.org/https://doi.org/10.1016/j.pmatsci.2015.06.003.

[21] X. Zhang, J. Hampshire, K. Cooke, X. Li, D. Pletcher, S. Wright, K. Hyde, High surface area coatings for hydrogen evolution cathodes prepared by magnetron sputtering, Int. J. Hydrogen Energy. 40 (2015) 2452–2459. https://doi.org/https://doi.org/10.1016/j.ijhydene.2014.12.107.

[22] J. Gil-Rostra, F.J. García-García, F.J. Ferrer, A.R. González-Elipe, F. Yubero, Microstructure of mixed oxide thin films prepared by magnetron sputtering at oblique angles, Thin Solid Films. 591 (2015) 330–335. https://doi.org/https://doi.org/10.1016/j.tsf.2015.01.058.

[23] J. Zhao, E. Baibuz, J. Vernieres, P. Grammatikopoulos, V. Jansson, M. Nagel, S. Steinhauer, M. Sowwan, A. Kuronen, K. Nordlund, F. Djurabekova, Formation Mechanism of Fe Nanocubes by Magnetron Sputtering Inert Gas Condensation, ACS Nano. 10 (2016) 4684–4694. https://doi.org/10.1021/acsnano.6b01024.

[24] S. Alvi, D.M. Jarzabek, M.G. Kohan, D. Hedman, P. Jenczyk, M.M. Natile, A. Vomiero, F. Akhtar, Synthesis and Mechanical Characterization of a

CuMoTaWV High-Entropy Film by Magnetron Sputtering, ACS Appl. Mater. Interfaces. 12 (2020) 21070–21079. https://doi.org/10.1021/acsami.0c02156.

[25] S. Hejazi, M. Altomare, S. Mohajernia, P. Schmuki, Composition Gradients in Sputtered Ti–Au Alloys: Site-Selective Au Decoration of Anodic TiO_2 Nanotubes for Photocatalytic H2 Evolution, ACS Appl. Nano Mater. 2 (2019) 4018–4025. https://doi.org/10.1021/acsanm.9b01022.

[26] I.V. Tudose, F. Comanescu, P. Pascariu, S. Bucur, L. Rusen, F. Iacomi, E. Koudoumas, M.P. Suchea, Chapter 2 - Chemical and physical methods for multifunctional nanostructured interface fabrication, in: V. Dinca, M.P.B.T.-F.N.I. for E. and B.A. Suchea (Eds.), Micro Nano Technol., Elsevier, 2019: pp. 15–26. https://doi.org/https://doi.org/10.1016/B978-0-12-814401-5.00002-5.

[27] C. Li, M. Iqbal, J. Lin, X. Luo, B. Jiang, V. Malgras, K.C.-W. Wu, J. Kim, Y. Yamauchi, Electrochemical Deposition: An Advanced Approach for Templated Synthesis of Nanoporous Metal Architectures, Acc. Chem. Res. 51 (2018) 1764–1773. https://doi.org/10.1021/acs.accounts.8b00119.

[28] A.Y. Faid, L. Xie, A.O. Barnett, F. Seland, D. Kirk, S. Sunde, Effect of anion exchange ionomer content on electrode performance in AEM water electrolysis, Int. J. Hydrogen Energy. 45 (2020) 28272–28284. https://doi.org/https://doi.org/10.1016/j.ijhydene.2020.07.202.

[29] I. Vincent, A. Kruger, D. Bessarabov, Development of efficient membrane electrode assembly for low cost hydrogen production by anion exchange membrane electrolysis, Int. J. Hydrogen Energy. 42 (2017) 10752–10761. https://doi.org/https://doi.org/10.1016/j.ijhydene.2017.03.069.

[30] B.G. Pollet, A.A. Franco, H. Su, H. Liang, S. Pasupathi, 1 - Proton exchange

membrane fuel cells, in: F. Barbir, A. Basile, T.N.B.T.-C. of H.E. Veziroğlu (Eds.), Woodhead Publ. Ser. Energy, Woodhead Publishing, Oxford, 2016: pp. 3–56. https://doi.org/https://doi.org/10.1016/B978-1-78242-363-8.00001-3.

[31] K. Nejati, S. Davari, A. Akbari, K. Asadpour-Zeynali, Z. Rezvani, A highly active oxygen evolution electrocatalyst: Ni-Fe-layered double hydroxide intercalated with the Molybdate and Vanadate anions, Int. J. Hydrogen Energy. 44 (2019) 14842–14852. https://doi.org/https://doi.org/10.1016/j.ijhydene.2019.04.045.

[32] D.A. Corrigan, The Catalysis of the Oxygen Evolution Reaction by Iron Impurities in Thin Film Nickel Oxide Electrodes, J. Electrochem. Soc. 134 (1987) 377–384. https://doi.org/10.1149/1.2100463.

[33] C. Niether, S. Faure, A. Bordet, J. Deseure, M. Chatenet, J. Carrey, B. Chaudret, A. Rouet, Improved water electrolysis using magnetic heating of FeC–Ni core–shell nanoparticles, Nat. Energy. 3 (2018) 476–483. https://doi.org/10.1038/s41560-018-0132-1.

[34] J. Gil-Rostra, M. Cano, J.M. Pedrosa, F.J. Ferrer, F. García-García, F. Yubero, A.R. González-Elipe, Electrochromic Behavior of WxSiyOz Thin Films Prepared by Reactive Magnetron Sputtering at Normal and Glancing Angles, ACS Appl. Mater. Interfaces. 4 (2012) 628–638. https://doi.org/10.1021/am2014629.

[35] R. Jervis, N. Mansor, A.J. Sobrido, S. Jones, C. Gibbs, T.P. Neville, J. Millichamp, P.R. Shearing, D.J.L. Brett, The Importance of Using Alkaline Ionomer Binders for Screening Electrocatalysts in Alkaline Electrolyte, J. Electrochem. Soc. 164 (2017) F1551–F1555. https://doi.org/10.1149/2.0441714jes.

[36] P. Fortin, T. Khoza, X. Cao, S.Y. Martinsen, A. Oyarce Barnett, S. Holdcroft, High-performance alkaline water electrolysis using Aemion[TM] anion exchange membranes, J. Power Sources. 451 (2020) 227814. https://doi.org/https://doi.org/10.1016/j.jpowsour.2020.227814.

[37] M. Carmo, G. Doubek, R.C. Sekol, M. Linardi, A.D. Taylor, Development and electrochemical studies of membrane electrode assemblies for polymer electrolyte alkaline fuel cells using FAA membrane and ionomer, J. Power Sources. 230 (2013) 169–175. https://doi.org/https://doi.org/10.1016/j.jpowsour.2012.12.015.

[38] A.K. Taylor, I. Andreu, B.D. Gates, Regular Dimpled Nickel Surfaces for Improved Efficiency of the Oxygen Evolution Reaction, ACS Appl. Energy Mater. 1 (2018) 1771–1782. https://doi.org/10.1021/acsaem.8b00338.

[39] M. Alsabet, M. Grdeń, G. Jerkiewicz, Electrochemical Growth of Surface Oxides on Nickel. Part 3: Formation of β-NiOOH in Relation to the Polarization Potential, Polarization Time, and Temperature, Electrocatalysis. 6 (2015) 60–71. https://doi.org/10.1007/s12678-014-0214-1.

[40] L. Trotochaud, S.L. Young, J.K. Ranney, S.W. Boettcher, Nickel–Iron Oxyhydroxide Oxygen-Evolution Electrocatalysts: The Role of Intentional and Incidental Iron Incorporation, J. Am. Chem. Soc. 136 (2014) 6744–6753. https://doi.org/10.1021/ja502379c.

[41] P. Thangavel, M. Ha, S. Kumaraguru, A. Meena, A.N. Singh, A.M. Harzandi, K.S. Kim, Graphene-nanoplatelets-supported NiFe-MOF: high-efficiency and ultra-stable oxygen electrodes for sustained alkaline anion exchange membrane water electrolysis, Energy Environ. Sci. 13 (2020) 3447–3458.

https://doi.org/10.1039/D0EE00877J.

[42] E. Cossar, A.O. Barnett, F. Seland, E.A. Baranova, The performance of nickel and nickel-iron catalysts evaluated as anodes in anion exchange membrane water electrolysis, Catalysts. 9 (2019). https://doi.org/10.3390/catal9100814.

[43] O. Diaz-Morales, D. Ferrus-Suspedra, M.T.M. Koper, The importance of nickel oxyhydroxide deprotonation on its activity towards electrochemical water oxidation, Chem. Sci. 7 (2016) 2639–2645. https://doi.org/10.1039/c5sc04486c.

[44] M. Balasubramanian, C.A. Melendres, S. Mini, X-ray Absorption Spectroscopy Studies of the Local Atomic and Electronic Structure of Iron Incorporated into Electrodeposited Hydrous Nickel Oxide Films, J. Phys. Chem. B. 104 (2000) 4300–4306. https://doi.org/10.1021/jp9921710.

[45] P. Axmann, O. Glemser, Nickel hydroxide as a matrix for unusual valencies: the electrochemical behaviour of metal(III)-ion-substituted nickel hydroxides of the pyroaurite type, J. Alloys Compd. 246 (1997) 232–241. https://doi.org/https://doi.org/10.1016/S0925-8388(96)02479-6.

[46] M. Louie, A. Bell, An Investigation of Thin-Film Ni-Fe Oxide Catalysts for the Electrochemical Evolution of Oxygen, J. Am. Chem. Soc. 135 (2013). https://doi.org/10.1021/ja405351s.

[47] D. Friebel, M.W. Louie, M. Bajdich, K.E. Sanwald, Y. Cai, A.M. Wise, M.-J. Cheng, D. Sokaras, T.-C. Weng, R. Alonso-Mori, R.C. Davis, J.R. Bargar, J.K. Nørskov, A. Nilsson, A.T. Bell, Identification of Highly Active Fe Sites in (Ni,Fe)OOH for Electrocatalytic Water Splitting, J. Am. Chem. Soc. 137 (2015) 1305–1313. https://doi.org/10.1021/ja511559d.

[48] G.B. Shombe, M.D. Khan, C. Zequine, C. Zhao, R.K. Gupta, N. Revaprasadu,

Direct solvent free synthesis of bare α-NiS, β-NiS and α-β-NiS composite as excellent electrocatalysts: Effect of self-capping on supercapacitance and overall water splitting activity, Sci. Rep. 10 (2020) 3260. https://doi.org/10.1038/s41598-020-59714-9.

[49]   A. Faid, F. Seland, S. Sunde, Optimized Nickel-Cobalt and Nickel-Iron Oxide Catalysts for the Hydrogen Evolution Reaction in Alkaline Water Electrolysis, J. Electrochem. Soc. 166 (2019) F519–F533. https://doi.org/10.1149/2.0821908jes.

[50]   K. . K, A. Sengeni, S. Ede, S. Kundu, Nanosheets of Nickel Iron Hydroxy Carbonate Hydrate with Pronounced OER Activity under Alkaline and Near-Neutral Conditions, Inorg. Chem. 58 (2019). https://doi.org/10.1021/acs.inorgchem.8b02680.

[51]   A.M.P. Sakita, E. Vallés, R. Della Noce, A. V Benedetti, Novel NiFe/NiFe-LDH composites as competitive catalysts for clean energy purposes, Appl. Surf. Sci. 447 (2018) 107–116. https://doi.org/https://doi.org/10.1016/j.apsusc.2018.03.235.

[52]   M.L. Lindstrom, R. Gakhar, K. Raja, D. Chidambaram, Facile Synthesis of an Efficient Ni-Fe-Co Based Oxygen Evolution Reaction Electrocatalyst, J. Electrochem. Soc. 167 (2020). https://doi.org/10.1149/1945-7111/ab6b08.

[53]   M. Sun, Z. Wang, B. Gao, S. Wang, C. Wang, X. Song, D. Lin, Electrocatalytic hydrogen evolution properties of anionic $NiS2-Ni(OH)_2$ nanosheets produced on the surface of nickel foam, Int. J. Energy Res. 44 (2020) 4827–4836. https://doi.org/10.1002/er.5275.

[54]   L. Wang, C.-Y. Lee, P. Schmuki, Solar water splitting: preserving the beneficial small feature size in porous $\alpha-Fe_2O_3$ photoelectrodes during annealing, J. Mater. Chem. A. 1 (2013) 212–215. https://doi.org/10.1039/C2TA00431C.

[55] R. Solmaz, G. Kardaş, Electrochemical deposition and characterization of NiFe coatings as electrocatalytic materials for alkaline water electrolysis, Electrochim. Acta. 54 (2009) 3726–3734. https://doi.org/https://doi.org/10.1016/j.electacta.2009.01.064.

[56] H. Zhang, X. Li, A. Hähnel, V. Naumann, C. Lin, S. Azimi, S.L. Schweizer, A.W. Maijenburg, R.B. Wehrspohn, Bifunctional Heterostructure Assembly of NiFe LDH Nanosheets on NiCoP Nanowires for Highly Efficient and Stable Overall Water Splitting, Adv. Funct. Mater. 28 (2018) 1706847. https://doi.org/https://doi.org/10.1002/adfm.201706847.

[57] M. Yu, G. Moon, E. Bill, H. Tüysüz, Optimizing Ni–Fe Oxide Electrocatalysts for Oxygen Evolution Reaction by Using Hard Templating as a Toolbox, ACS Appl. Energy Mater. 2 (2019) 1199–1209. https://doi.org/10.1021/acsaem.8b01769.

[58] S. Watzele, P. Hauenstein, Y. Liang, S. Xue, J. Fichtner, B. Garlyyev, D. Scieszka, F. Claudel, F. Maillard, A.S. Bandarenka, Determination of Electroactive Surface Area of Ni-, Co-, Fe-, and Ir-Based Oxide Electrocatalysts, ACS Catal. 9 (2019) 9222–9230. https://doi.org/10.1021/acscatal.9b02006.

[59] P. Shinde, C.S. Rout, D. Late, P.K. Tyagi, M.K. Singh, Optimized performance of nickel in crystal-layered arrangement of NiFe2O4/rGO hybrid for high-performance oxygen evolution reaction, Int. J. Hydrogen Energy. 46 (2021) 2617–2629. https://doi.org/https://doi.org/10.1016/j.ijhydene.2020.10.144.

[60] H.A. Bandal, A.R. Jadhav, H. Kim, Facile synthesis of bicontinuous Ni3Fe alloy for efficient electrocatalytic oxygen evolution reaction, J. Alloys Compd. 726 (2017) 875–884. https://doi.org/10.1016/j.jallcom.2017.07.290.

[61]   J. Wang, W. Zhang, Z. Zheng, J. Liu, C. Yu, Y. Chen, K. Ma, Dendritic core-shell Ni@Ni(Fe)OOH metal/metal oxyhydroxide electrode for efficient oxygen evolution reaction, Appl. Surf. Sci. 469 (2019) 731–738. https://doi.org/10.1016/j.apsusc.2018.10.232.

[62]   L. Xu, L. Cao, W. Xu, Z. Pei, One-step electrosynthesis of NiFe-NF electrodes for highly efficient overall water splitting, Appl. Surf. Sci. 503 (2020). https://doi.org/10.1016/j.apsusc.2019.144122.

[63]   D.H. Youn, Y.B. Park, J.Y. Kim, G. Magesh, Y.J. Jang, J.S. Lee, One-pot synthesis of NiFe layered double hydroxide/reduced graphene oxide composite as an efficient electrocatalyst for electrochemical and photoelectrochemical water oxidation, J. Power Sources. 294 (2015) 437–443. https://doi.org/10.1016/j.jpowsour.2015.06.098.

[64]   A.W. Hull., A New Method of X-Ray Crystal Analysis, Phys. Rev. 10 (1917) 661–696. https://doi.org/10.1103/PhysRev.10.661.

[65]   J.D. Hanawalt, H.W. Rinn, L.K. Frevel, Chemical Analysis by X-Ray Diffraction, Ind. Eng. Chem. Anal. Ed. 10 (1938) 457–512. https://doi.org/10.1021/ac50125a001.

[66]   C.-C. Hu, Y.-R. Wu, Bipolar performance of the electroplated iron–nickel deposits for water electrolysis, Mater. Chem. Phys. 82 (2003) 588–596. https://doi.org/https://doi.org/10.1016/S0254-0584(03)00316-X.

[67]   L. Luo, X. Han, Q. Zeng, Hydrogenative Cyclization of Levulinic Acid to γ-Valerolactone with Methanol and Ni-Fe Bimetallic Catalysts, Catal. . 10 (2020). https://doi.org/10.3390/catal10091096.

[68]   E. Navarro-Flores, Z. Chong, S. Omanovic, Characterization of Ni, NiMo, NiW

and NiFe electroactive coatings as electrocatalysts for hydrogen evolution in an acidic medium, J. Mol. Catal. A Chem. 226 (2005) 179–197. https://doi.org/https://doi.org/10.1016/j.molcata.2004.10.029.

[69] Standard X-Ray Diffraction Powder Patterns, Nature. 176 (1955) 147. https://doi.org/10.1038/176147a0.

[70] Z. Hajizadeh, F. Radinekiyan, R. Eivazzadeh-keihan, A. Maleki, Development of novel and green NiFe2O4/geopolymer nanocatalyst based on bentonite for synthesis of imidazole heterocycles by ultrasonic irradiations, Sci. Rep. 10 (2020) 11671. https://doi.org/10.1038/s41598-020-68426-z.

[71] N. Iranpour Anaraki, R. Poursalehi, Shielding Effectiveness of Polymeric Nanocomposites Filled with Iron/Wüstite Nanoparticles, Procedia Mater. Sci. 11 (2015) 700–705. https://doi.org/10.1016/j.mspro.2015.11.041.

[72] O. Butenko, V. Boychuk, B. Savchenko, V. Kotsyubynsky, V. Khomenko, V. Barsukov, Pure ultrafine magnetite from carbon steel wastes, Mater. Today Proc. 6 (2019) 270–278. https://doi.org/10.1016/j.matpr.2018.10.104.

[73] E. Tronc, C. Chanéac, J.P. Jolivet, Structural and Magnetic Characterization ofε-Fe2O3, J. Solid State Chem. 139 (1998) 93–104. https://doi.org/https://doi.org/10.1006/jssc.1998.7817.

[74] T. Blomberg, T. Tripathi, M. Karppinen, New chemical mechanism explaining the breakdown of protective oxides on high temperature steels in biomass combustion and gasification plants, RSC Adv. 9 (2019) 10034–10048. https://doi.org/10.1039/C9RA00582J.

[75] Q. Xu, H. Jiang, X. Duan, Z. Jiang, Y. Hu, S.W. Boettcher, W. Zhang, S. Guo, C. Li, Fluorination-enabled Reconstruction of NiFe Electrocatalysts for Efficient

Water Oxidation, Nano Lett. 21 (2021) 492–499. https://doi.org/10.1021/acs.nanolett.0c03950.

[76] C. Andronescu, S. Seisel, P. Wilde, S. Barwe, J. Masa, Y.-T. Chen, E. Ventosa, W. Schuhmann, Influence of Temperature and Electrolyte Concentration on the Structure and Catalytic Oxygen Evolution Activity of Nickel–Iron Layered Double Hydroxide, Chem. – A Eur. J. 24 (2018) 13773–13777. https://doi.org/https://doi.org/10.1002/chem.201803165.

[77] S. Ahn, B.-S. Lee, I. Choi, S. Yoo, H.-J. Kim, E. Cho, D. Henkensmeier, S. Nam, J. Jang, Development of a membrane electrode assembly for alkaline water electrolysis by direct electrodeposition of nickel on carbon papers, Appl. Catal. B Environ. 154–155 (2014) 197–205. https://doi.org/10.1016/j.apcatb.2014.02.021.

[78] A. Caravaca, A. De Lucas-Consuegra, A.B. Calcerrada, J. Lobato, J.L. Valverde, F. Dorado, From biomass to pure hydrogen: Electrochemical reforming of bio-ethanol in a PEM electrolyser, Appl. Catal. B Environ. 134–135 (2013) 302–309. https://doi.org/10.1016/j.apcatb.2013.01.033.

[79] W. Wu, J. Liu, N. Johannes, Electrodeposition of Ir–Co thin films on copper foam as high-performance electrocatalysts for efficient water splitting in alkaline medium, Int. J. Hydrogen Energy. 46 (2021) 609–621. https://doi.org/https://doi.org/10.1016/j.ijhydene.2020.09.268.

[80] V.M. Nikolic, S.L. Maslovara, G.S. Tasic, T.P. Brdaric, P.Z. Lausevic, B.B. Radak, M.P. Marceta Kaninski, Kinetics of hydrogen evolution reaction in alkaline electrolysis on a Ni cathode in the presence of Ni–Co–Mo based ionic activators, Appl. Catal. B Environ. 179 (2015) 88–94. https://doi.org/https://doi.org/10.1016/j.apcatb.2015.05.012.

[81] A. Rodríguez-Gómez, F. Dorado, A. de Lucas-Consuegra, A.R. de la Osa, Influence of the GDL and assembly mode of a PEM cell on the ethanol revalorization into chemicals, Chem. Eng. J. 402 (2020) 125298. https://doi.org/https://doi.org/10.1016/j.cej.2020.125298.

[82] E. Amores, J. Rodríguez, J. Oviedo, A. Lucas-Consuegra, Development of an operation strategy for hydrogen production using solar PV energy based on fluid dynamic aspects, Open Eng. 7 (2017). https://doi.org/10.1515/eng-2017-0020.

[83] J. Parrondo, C.G. Arges, M. Niedzwiecki, E.B. Anderson, K.E. Ayers, V. Ramani, Degradation of anion exchange membranes used for hydrogen production by ultrapure water electrolysis, RSC Adv. 4 (2014) 9875–9879. https://doi.org/10.1039/C3RA46630B.

[84] P. Ganesan, A. Sivanantham, S. Shanmugam, Nanostructured Nickel–Cobalt–Titanium Alloy Grown on Titanium Substrate as Efficient Electrocatalyst for Alkaline Water Electrolysis, ACS Appl. Mater. Interfaces. 9 (2017) 12416–12426. https://doi.org/10.1021/acsami.7b00353.

[85] L. Xiao, S. Zhang, J. Pan, C. Yang, M. He, L. Zhuang, J. Lu, First implementation of alkaline polymer electrolyte water electrolysis working only with pure water, Energy Environ. Sci. 5 (2012) 7869–7871. https://doi.org/10.1039/C2EE22146B.

[86] D. Xu, M.B. Stevens, M.R. Cosby, S.Z. Oener, A.M. Smith, L.J. Enman, K.E. Ayers, C.B. Capuano, J.N. Renner, N. Danilovic, Y. Li, H. Wang, Q. Zhang, S.W. Boettcher, Earth-Abundant Oxygen Electrocatalysts for Alkaline Anion-Exchange-Membrane Water Electrolysis: Effects of Catalyst Conductivity and Comparison with Performance in Three-Electrode Cells, ACS Catal. 9 (2019) 7–

15. https://doi.org/10.1021/acscatal.8b04001.

[87] A.S. Aricò, M. Girolamo, S. Siracusano, D. Sebastian, V. Baglio, M. Schuster, Polymer Electrolyte Membranes for Water Photo-Electrolysis, Membranes (Basel). 7 (2017) 25. https://doi.org/10.3390/membranes7020025.

[88] G. Gupta, K. Scott, M. Mamlouk, Performance of polyethylene based radiation grafted anion exchange membrane with polystyrene-b-poly (ethylene/butylene)-b-polystyrene based ionomer using NiCo2O4 catalyst for water electrolysis, J. Power Sources. 375 (2018) 387–396. https://doi.org/https://doi.org/10.1016/j.jpowsour.2017.07.026.

[89] J. Hnát, M. Plevova, R.A. Tufa, J. Zitka, M. Paidar, K. Bouzek, Development and testing of a novel catalyst-coated membrane with platinum-free catalysts for alkaline water electrolysis, Int. J. Hydrogen Energy. 44 (2019) 17493–17504. https://doi.org/https://doi.org/10.1016/j.ijhydene.2019.05.054.

[90] A. Carbone, S.C. Zignani, I. Gatto, S. Trocino, A.S. Aricò, Assessment of the FAA3-50 polymer electrolyte in combination with a $NiMn_2O_4$ anode catalyst for anion exchange membrane water electrolysis, Int. J. Hydrogen Energy. 45 (2020) 9285–9292. https://doi.org/https://doi.org/10.1016/j.ijhydene.2020.01.150.

[91] S.M. Park, M.J. Jang, Y.S. Park, J. Lee, J.-Y. Jeong, J. Jung, M.-K. Choi, Y.-S. Noh, M.-H. Seo, H.J. Kim, J. Yang, Y.D. Kim, S.M. Choi, Synthesis and characterization of the $Cu_{0.72}CO_{2.28}O_4$ catalyst for oxygen evolution reaction in an anion exchange membrane water electrolyzer, J. Korean Inst. Met. Mater. 58 (2020) 49–58. https://doi.org/10.3365/KJMM.2020.58.1.49.

[92] Y.S. Park, M.J. Jang, J. Jeong, S.M. Park, X. Wang, M.H. Seo, S.M. Choi, J. Yang, Hierarchical Chestnut-Burr like Structure of Copper Cobalt Oxide

Electrocatalyst Directly Grown on Ni Foam for Anion Exchange Membrane Water Electrolysis, ACS Sustain. Chem. Eng. (2020). https://doi.org/10.1021/acssuschemeng.9b06767.

[93] W. Guo, J. Kim, H. Kim, S.H. Ahn, Cu–Co–P electrodeposited on carbon paper as an efficient electrocatalyst for hydrogen evolution reaction in anion exchange membrane water electrolyzers, Int. J. Hydrogen Energy. (2021). https://doi.org/https://doi.org/10.1016/j.ijhydene.2021.03.120.